

## Defect enhanced funneling of diffusion current in silicon

S. Azimi,<sup>1</sup> Z. Y. Dang,<sup>1</sup> J. Song,<sup>1</sup> M. B. H. Breese,<sup>1,a)</sup> E. Vittone,<sup>2</sup> and J. Forneris<sup>2</sup>

<sup>1</sup>Department of Physics, Centre for Ion Beam Applications (CIBA), National University of Singapore, Singapore 117542

<sup>2</sup>Physics Department, NIS Excellence Centre and CNISM, University of Torino, via Pietro Giuria 1, 10125 Torino, Italy

(Received 8 November 2012; accepted 10 January 2013; published online 29 January 2013)

We report a current transport mechanism observed during electrochemical anodization of ion irradiated p-type silicon, in which a hole diffusion current is highly funneled along the gradient of modified doping profile towards the maximum ion induced defect density, dominating the total current flowing and hence the anodization behaviour. This study is characterized within the context of electrochemical anodization but relevant to other fields where any residual defect density may result in similar effects, which may adversely affect performance, such as in wafer gettering or satellite-based microelectronics. Increased photoluminescence intensity from localized buried regions of porous silicon is also shown. © 2013 American Institute of Physics. [<http://dx.doi.org/10.1063/1.4789849>]

Electrochemical anodization of silicon results in porous silicon formation<sup>1,2</sup> used for producing sensors,<sup>3,4</sup> utilizing the photoluminescence properties of porous silicon<sup>5–7</sup> and as sacrificial material for micro-electro-mechanical systems (MEMS) or silicon photonics.<sup>8–10</sup> Electrochemical patterning of silicon may be achieved in various ways, e.g., deeply etched arrays of pores in high resistivity wafers are produced with a wall thickness determined by the space charge region.<sup>11</sup> Modulating the anodization current allows three dimensional fabrication of photonic lattices.<sup>12–14</sup>

The generation of ion induced defects in silicon depends on many factors; typical defects produced are divacancies and other vacancy or impurity-related centres. Many defects act as trap levels where charge carriers undergo recombination. Electrochemical patterning of p-type silicon using high-fluence ion irradiation is achieved by reducing the effective acceptor concentration,<sup>15</sup> resulting in a reduced anodization current by partially or fully depleting these regions.<sup>16,17</sup> Silicon micromachining using high-fluence, high-energy ion irradiation enables the formation of micro- and nano-scale wires, surface and three dimensional patterning,<sup>10,17,18</sup> and components for silicon photonics.<sup>9,19,20</sup> However, the underlying current transport and porous silicon formation mechanism of electrochemically anodized, ion irradiated, p-type silicon has not been completely investigated. A better understanding of such current flow would enable easier formation of nano- and micro-silicon wires and porous silicon structures and applications based on this approach,<sup>9,10,17–20</sup> while also providing valuable insight in all fields related to charge particle irradiation of semiconductor materials, such as in Refs. 21–28.

Here, we report a current transport mechanism observed during electrochemical anodization of ion irradiated p-type silicon, which dominates the total current flowing and hence the anodization behavior in localized areas. It is shown how low-fluence ion irradiation of p-type silicon causes an acceptor doping gradient around the irradiated region. During subsequent electrochemical anodization, this results in funneling of

the hole diffusion current along the gradient of modified doping profile towards the minimum doping density which dominates the anodization behaviour. This is observed both for low energy ions where the maximum of the Bragg nuclear energy loss is close to the surface, and for high energy ions where the Bragg maximum is several microns beneath the surface. This phenomenon enables fabrication of porous silicon in selective areas with much higher photoluminescence compared with the surrounding material and reduces cracking problems which may have further applications.<sup>30,31</sup> This study is described within the context of electrochemical anodization but is relevant to other fields where any residual defect density may result in similar funneling effects, which may adversely affect performance, such as in satellite-based devices,<sup>21,22</sup> proton isolation of device areas,<sup>23,24</sup> wafer gettering,<sup>25–27</sup> and ion irradiation of wide band gap semiconductors.<sup>28</sup>

Consider a regime where the defect distribution across the ion end-of-range region is much wider than at the irradiated surface. The most relevant irradiation parameter is the *line fluence*  $\Psi$ , i.e., the number of ions irradiating a zero-width line per centimetre of line length.<sup>10</sup> We mainly consider  $0.4 \text{ } \Omega \cdot \text{cm}$  (acceptor density  $N_A = 4.8 \cdot 10^{16} \text{ cm}^{-3}$ ) silicon but also demonstrate diffusion current funneling in  $0.02 \text{ } \Omega \cdot \text{cm}$  silicon.

Figure 1 shows Atomic force microscope (AFM) images of the etched surface profile for line irradiations with 34 keV He ions, focused to  $\sim 1 \text{ nm}$  in a helium ion microscope.<sup>29</sup> At low energies, the maximum of the Bragg peak of nuclear energy loss is close to the surface.<sup>32,33</sup> Groups of five lines were irradiated with different  $\Psi$ , then the sample was anodized to a depth of  $\sim 150 \text{ nm}$  with a current density of  $60 \text{ mA/cm}^2$  in a solution of 24% HF for 4 s. A line period of 700 nm is sufficiently large to ensure that the lines anodize independently, except for the highest fluence where a larger period was used.

At the lowest fluence ( $\Psi = 6 \times 10^7/\text{cm}$ ), there are peaks of  $\sim 200 \text{ nm}$  full-width-at-half-maximum (FWHM) at the irradiated lines, indicating a lower local anodization current density than that flowing through the surrounding, unirradiated silicon, consistent with the defects deflecting away the anodization current.<sup>16,17</sup> While a similar peak width is

<sup>a)</sup>Author to whom correspondence should be addressed. Electronic mail: phymbhb@nus.edu.sg.

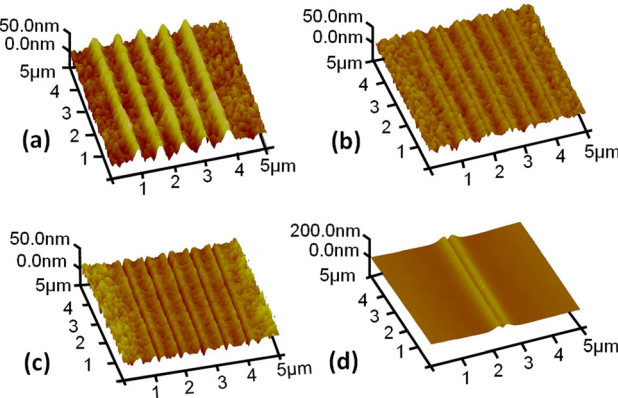


FIG. 1. AFM images of lines in  $0.4 \Omega \text{ cm}$  p-type type silicon irradiated with 34 keV He ions with a period of 700 nm, with (a)  $\Psi = 6 \times 10^7/\text{cm}^2$ , (b)  $3 \times 10^8/\text{cm}^2$ , (c)  $6 \times 10^8/\text{cm}^2$ . (d) Period of 5  $\mu\text{m}$  for  $\Psi = 2 \times 10^{10}/\text{cm}^2$ . After anodization, oxidation at  $800^\circ\text{C}$  for 20 min and immersion in a 2% HF solution is used to remove oxidised porous silicon.

observed for increasing  $\Psi$ , a dip of  $\sim 80$  nm FWHM is superposed on it, becoming more pronounced at higher fluences. These results suggest that current is increasingly funneled towards the maximum defect density with increasing fluence, creating a high, localized current density which counteracts the tendency of defects to deflect away the hole current.

Fig. 2 shows the effect of different fluences of 500 keV protons focused to 200 nm in a nuclear microprobe.<sup>34</sup> This energy is higher than the Bragg peak, so the maximum defect density occurs towards the end-of-range which is several micrometers beneath the surface. In Fig. 2(a), formation of a solid silicon core at the end-of range is observed at  $\Psi = 3.5 \times 10^{10}/\text{cm}^2$ ; at higher fluences, the core expands and extends towards the surface, following the higher defect distribution. The dark, faint region surrounding and above these cores is interpreted as high porosity silicon, which is more insulating, so emitting fewer secondary electrons than surrounding lower porosity silicon in SEM images. At lower  $\Psi$ , the core size reduces towards zero, leaving another faint, dark region, similarly interpreted as high porosity silicon produced by increased current density flowing into these regions. This is observed down to  $\Psi = 5 \times 10^8/\text{cm}^2$ , two orders of magnitude below the minimum fluence for forming

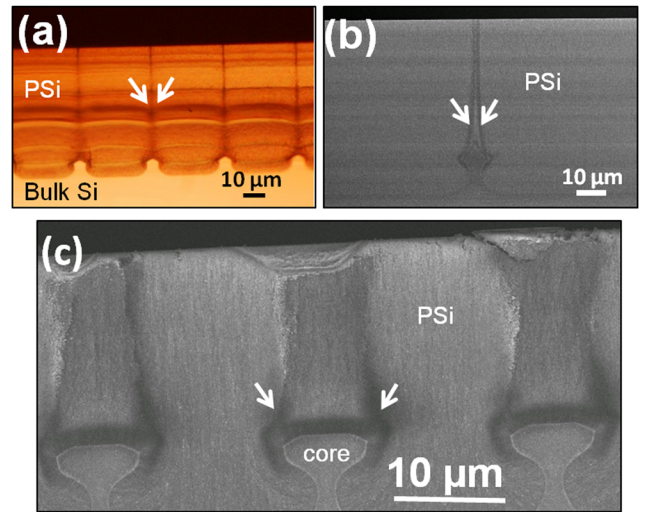


FIG. 3. Cross-section (a) optical and (b), (c) SEM images of irradiated  $0.02 \Omega \text{ cm}$  p-type silicon cleaved for imaging: (a) irradiated with 2 MeV proton  $\Psi = 1.6 \times 10^{11}/\text{cm}^2$ , then anodized to a depth of 50  $\mu\text{m}$ ; (b) irradiated with 2 MeV proton  $\Psi = 2 \times 10^{12}/\text{cm}^2$ , then anodized to a depth of 60  $\mu\text{m}$ ; (c) 10  $\mu\text{m}$  irradiated width with 1 MeV proton  $\Psi = 1 \times 10^{15}/\text{cm}^2$ , then anodized to a depth of 30  $\mu\text{m}$ .

a solid core. The cores formed at high  $\Psi$  are clearly seen in Fig. 2(b) and increased photoluminescence (PL) is observed in Fig. 2(c) from all dark regions surrounding and above them in Fig. 2(a), and the end-of-range at low  $\Psi$ . Fig. 2(c) insets shows PL around the solid cores increased by a factor of  $\sim 7$  and increased by a lesser amount at the low  $\Psi$  end-of-range, which is consistent with the anodization current being funnelled into these regions.

Figure 3(a) shows lines irradiated with a high  $\Psi$  in 0.02  $\Omega \text{ cm}$  p-type silicon. An alternating high/low current density was used to produce bright/dark porous layers owing to the strong variations in porosity which can be induced in such low resistivity silicon (Ref. 1, page 111), allowing the evolution of the etch front to be followed in time and depth. The line fluence is high enough for cores to form at the end-of-range, but of particular interest here is the profile of the etch front, which clearly curves downwards close to the dark columns of the irradiated lines (arrows show one example), indicating more rapid etching towards the irradiated

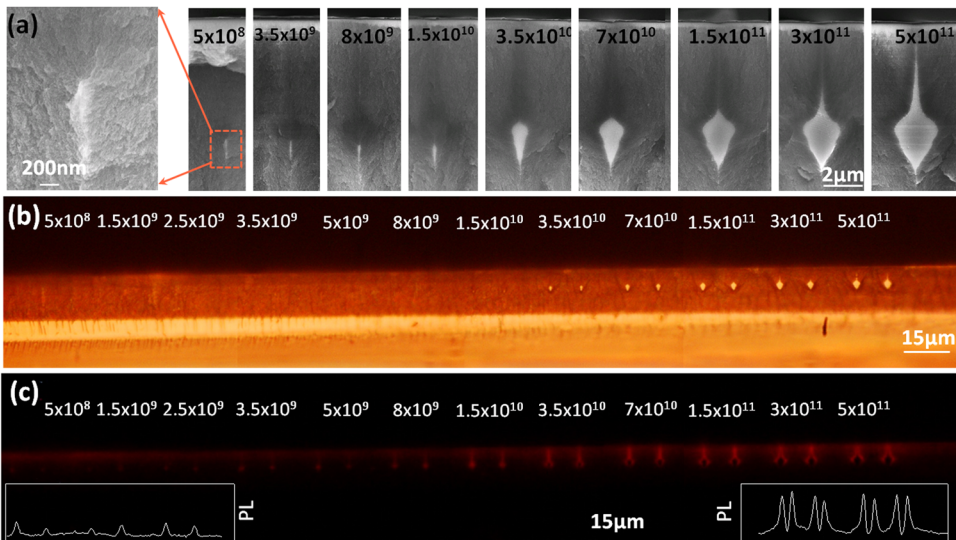


FIG. 2. (a) Cross-section SEM showing lines irradiated with 500 keV protons with different  $\Psi$  in  $0.4 \Omega \text{ cm}$  silicon, anodized with a current density of  $40 \text{ mA/cm}^2$  to a depth of 30  $\mu\text{m}$ . A higher magnification of the lowest  $\Psi$  is shown at the left. (b) Optical and (c) PL images of the same lines. PL was excited using a wavelength of 330 to 380 nm and the image was collected for 50 ms. The insets in (c) show PL intensity across the lowest and highest  $\Psi$  cores.

lines. By a closer look at the different contrast within the porous silicon along the ion trajectory in  $0.02 \Omega$  cm p-type silicon, Figs. 3(b) and 3(c) show a darker region at the boundary between the irradiated and unirradiated zones (indicated by arrows) in both cases, across which one expects a defect density gradient, whereas in the central portion of this irradiated region, one expects a constant defect density.

To understand these experimental results, simulations of the hole current flow through and around ion irradiated areas in  $0.4 \Omega$  cm p-type silicon were performed to characterize the drift and diffusion currents during anodization. We recognize that these simulations are an imperfect guide as they take no account of the actual interface between the silicon and electrolyte where anodization occurs or time evolution of the etch front.

The effects of ion irradiation were modelled for single and multiple line irradiations of different fluences. The average two dimensional vacancy density per single ion,  $v_G(x, y)$ , generated by a point focus of 30 keV He ions is shown in Fig. 4(a), calculated by convolution of the vacancy density from a delta-like point source using Stopping and Range of Ions in Matter (SRIM2010),<sup>32,33</sup> assuming a displacement energy of 20 eV. As expected, the maximum vacancy density occurs at, or very close to, the surface for low ion energies.

The final two dimensional vacancy density generated by a fluence  $\Psi$  is given by  $N_A^{\text{eff}}(x, y) = v_G(x, y) \cdot \Psi$ . We assume the vacancy distribution in the irradiated silicon reduces the acceptor concentration  $N_A$  by a fraction,  $f$ , of the vacancies behaving as donors,<sup>35,36</sup> so compensating the native acceptor concentration, giving an effective acceptor concentration  $N_A^{\text{eff}}$  (Ref. 37)

$$N_A^{\text{eff}} = N_A - f \cdot \Psi v_G(x, y) = N_A - f \cdot V_G(x, y). \quad (1)$$

This assumes a linear relationship between the density of traps which are generated by ions and the density of vacancies (though a non-linear relationship is possible). To vary  $N_A^{\text{eff}}$  one could change either  $f$  or  $\Psi$ ; we use a fixed value of  $f = 10^{-4}$  and vary  $\Psi$ , for easier comparison with experimental results. This  $f$  value is consistent with previous studies by other groups on effects of ion irradiation on electrical properties of silicon.<sup>15,38–40</sup> The map of  $N_A^{\text{eff}}$  for  $\Psi = 4 \times 10^8 / \text{cm}^2$  follows that of the vacancy density but with the minimum  $N_A^{\text{eff}}$  at the surface where the maximum defect density is located.

Evaluation of the two-dimensional hole current flowing around irradiated regions under an applied potential  $V_{\text{bias}}$  was performed by solving the Poisson's and continuity equation using a finite element method package. The simulation

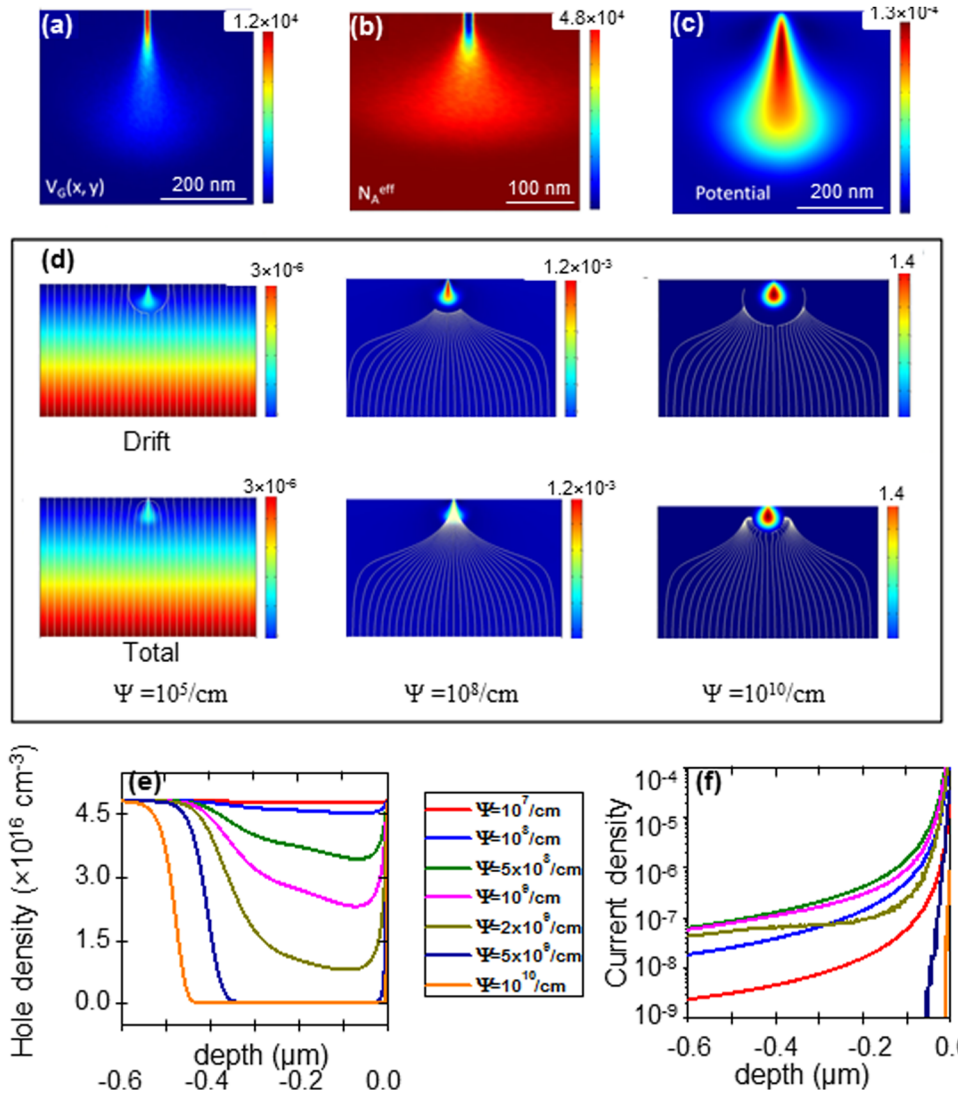


FIG. 4. (a) SRIM map of the average vacancy distribution  $v_G(x, y)$  ( $\mu\text{m}^{-2}$ ) per 30 keV  $\text{He}^+$  in silicon. (b)  $N_A^{\text{eff}}$  ( $\mu\text{m}^{-3}$ ) map for  $\Psi = 4 \times 10^8 / \text{cm}^2$  in  $0.4 \Omega$  cm silicon. (c) Electric potential map for  $\Psi = 1 \times 10^7 / \text{cm}^2$ . (a)–(c) have a vertical box size of  $0.5 \mu\text{m}$ . (d) Potential (color scale on the right) and current streamlines for (upper) drift component and (lower) total current flow for increasing values of  $\Psi$ . The horizontal  $\times$  vertical box size is  $3 \times 2 \mu\text{m}^2$ . (e) Hole density and (f) total current density versus depth at the symmetry axis, for different  $\Psi$ . The legend in the centre is common to both.

only deals with majority carriers and we assume a negligible recombination of holes in the irradiated region. Irradiation modifies the effective fixed charge profile, inducing a local reduction of the hole density and generating a partially/fully depleted region at low/high  $\Psi$ . The top and bottom boundaries were considered of the Dirichlet type (Ohmic contacts), with a constant positive potential,  $V_{\text{bias}}$ , at the bottom surface and the top surface grounded.

A total current density comprising the sum of the drift and diffusion currents of  $40 \text{ mA/cm}^2$  flowing through a  $500 \mu\text{m}$  thick wafer was assumed. A domain thickness of  $2 \mu\text{m}$  was used, giving an equivalent value of  $V_{\text{bias}} = 3.2 \times 10^{-6} \text{ V}$ . Fig. 4(c) shows the map of the positive electric potential at an irradiated region for  $\Psi = 1 \times 10^7/\text{cm}$ , from which one expects a hole drift current to be repelled during anodization.

Fig. 4(d) shows simulations for the (upper) drift component and (lower) total hole current (sum of the drift and diffusion components) for different  $\Psi$ . As expected, the drift current is increasingly repelled from the irradiated region with increasing  $\Psi$ , due to a larger positive electric potential. At the lowest fluence, the total current is very weakly funnelled at the surface, with this effect disappearing at depths greater than  $\sim 100 \text{ nm}$ , hence this effect is not observed in Fig. 1(a) where the deflection of the drift component from the irradiated area dominates the observed behaviour for an etch depth of  $\sim 150 \text{ nm}$ . At  $\Psi = 1 \times 10^8/\text{cm}$ , the total hole current is highly concentrated towards a narrow surface region because the diffusion component is funnelled over both a large lateral and depth range into a highly localized current density which dominates the anodization behaviour. At  $\Psi \sim 1 \times 10^{10}/\text{cm}$ , current transport through the irradiated region reduces to zero, resulting in the formation of a solid core. Changes in hole mobility due to additional ion-induced scattering centres were included but were found to vary little for the low  $\Psi$  over which diffusion funneling was observed.

Figs. 4(e) and 4(f), respectively, plot the hole density and total anodization current density (vertical component) versus depth below the surface at the irradiated line centre, giving insights into the mechanism which drives the current funneling observed in the above results. In Fig. 4(e), the hole density changes from high to low on moving towards the surface, the gradient increasing with  $\Psi$  (up to  $\Psi \leq 2 \times 10^9/\text{cm}$ ). One observes a correlation between the hole density gradient and an increasing total anodization current density with increasing  $\Psi$ ; clearly, the gradient of the hole concentration is responsible for funneling the hole diffusion component towards the maximum defect density, at the surface in this case. At higher  $\Psi$ , the irradiated depth is largely depleted of holes and current transport through this region rapidly reduces to zero. Current funneling is still observed at the outer zone surrounding the resultant core where the gradient of the hole concentration is large.

Fig. 5 shows simulations for high energy protons ( $250 \text{ keV}$ , range  $\sim 2.4 \mu\text{m}$ ), showing the potential map with superposed hole current streamlines for  $\Psi = 10^{10}/\text{cm}$  and  $10^{11}/\text{cm}$ . This proton energy is well above the Bragg peak for nuclear energy loss, hence the defect density reaches a maximum well beneath the surface at the end-of-range, along with the minimum hole density and the maximum

electric potential, with weaker effects along the initial portion of the ion trajectory where the defect density is about ten times lower.

Repulsion of the drift current from the defect induced potential at the end-of-range is clearly seen. At low fluence, holes still penetrate the end-of-range potential barrier and diffuse towards the minimum  $N_A^{\text{eff}}$  density. Diffusion combined with the repulsion by the electric field leads to current funneling of holes around the damage region, consistent with higher porosity of the silicon surrounding and above the core observed in Fig. 2.

For higher fluences, the electrical repulsion produces a more effective hole current deflection around highly damaged regions, resulting in expansion of the core, through which hole current streamlines cannot pass. Moreover, the horizontal component of the electric field repels holes from the ion track. Consequently, the hole current does not cross the elongated damaged region above the core and the streamlines deflected by the core potential run parallel to the damage profile and are funnelled upward. This is consistent with Fig. 2(a): at high fluence, the core remains unaffected by anodization and extends along an upward sharp protuberance corresponding to the ion track.

Funneling of the anodization current into the ion trajectory is consistent with the enhanced etching rate seen in Fig. 3(a). Further evidence of the importance of the defect-induced doping density gradient being responsible for the funneling and enhancement of the diffusion current is seen by the darker contrast porous silicon observed at the boundaries between the irradiated and unirradiated regions in Figs. 3(b) and 3(c) compared to the central, lighter-coloured porous regions where the absence of the doping gradient reduces the resultant current flow.

In conclusion, we have observed a transport mechanism whereby ion irradiation induces a hole diffusion current towards the maximum defect density. This is funnelled by the modified doping profile and can dominate the total current flowing. It indicates that any charged particle irradiation or implantation process where a residual defect density remains may be subject to unsuspected large, localized currents which may adversely affect performance.

M.B. and E.V. wish to thank the International Atomic Energy Agency for partial support under the CRP project number F11016.

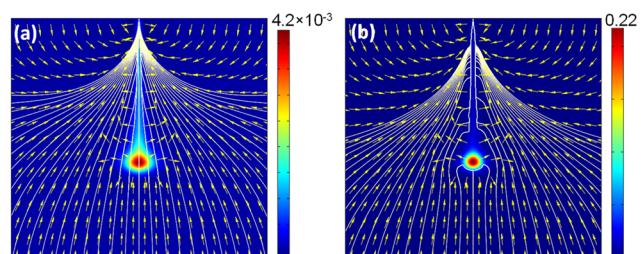


FIG. 5. Simulations for  $250 \text{ keV}$  proton line irradiation in  $0.4 \Omega \text{ cm}$  silicon, (a)  $\Psi = 10^{10}/\text{cm}$ , (b)  $\Psi = 10^{11}/\text{cm}$ , showing potential maps with superposed hole current streamlines; arrows indicate direction of the electric field (the arrow length is normalized, so not proportional to the field strength). The horizontal  $\times$  vertical box size is  $4 \times 4 \mu\text{m}^2$ .

- <sup>1</sup>V. Lehmann, *Electrochemistry of Silicon: Instrumentation, Science, Materials and Applications* (Wiley-VCH, New York, 2002).
- <sup>2</sup>M. J. Sailor, *Porous Silicon in Practice: Preparation, Characterization and Applications* (Wiley-VCH, Weinheim, 2011).
- <sup>3</sup>V. S.-Y. Lin, K. Motesharei, K. S. Dancil, M. J. Sailor, and M. R. Ghadiri, *Science* **278**, 840 (1997).
- <sup>4</sup>B. H. King, A. M. Ruminski, J. L. Snyder, and M. J. Sailor, *Adv. Mater.* **19**, 4530 (2007).
- <sup>5</sup>F. Ramiro-Manzano, R. Fenollosa, E. Xifré-Pérez, M. Garinand, and F. Mesegue, *Adv. Mater.* **23**, 3022 (2011).
- <sup>6</sup>E. J. Teo, M. B. H. Breese, A. A. Bettoli, D. Mangaiyarkarasi, F. Champeaux, F. Watt, and D. Blackwood, *Adv. Mater.* **18**, 51 (2006).
- <sup>7</sup>E. J. Teo, D. Mangaiyarkarasi, M. B. H. Breese, A. A. Bettoli, and D. J. Blackwood, *Appl. Phys. Lett.* **85**, 4370 (2004).
- <sup>8</sup>Y. Ding, Z. Liu, L. Liu, and Z. Li, *Microsyst. Technol.* **9**, 470 (2003).
- <sup>9</sup>E. J. Teo, A. A. Bettoli, P. Yang, M. B. H. Breese, B. Q. Xiong, G. Z. Mashanovich, W. R. Headley, and G. T. Reed, *Opt. Lett.* **34**, 659 (2009).
- <sup>10</sup>S. Azimi, M. B. H. Breese, Z. Y. Dang, Y. Yan, Y. S. Ow, and A. A. Bettoli, *J. Micromech. Microeng.* **22**, 015015 (2012).
- <sup>11</sup>V. Lehmann, *J. Electrochem. Soc.* **140**, 2836 (1993).
- <sup>12</sup>M. Bassu, S. Surdo, L. M. Strambini, and G. Barillaro, *Adv. Funct. Mater.* **22**, 1222 (2012).
- <sup>13</sup>S. Matthias, F. Müller, and U. Gösele, *J. Appl. Phys.* **98**, 023524 (2005).
- <sup>14</sup>S. Matthias, F. Müller, C. Jamois, R. B. Wehrspohn, and U. Gösele, *Adv. Mater.* **16**, 2166 (2004).
- <sup>15</sup>M. Yamaguchi, S. J. Taylor, M. J. Yang, S. Matsuda, O. Kawasaki, and T. Hisamatsu, *J. Appl. Phys.* **80**, 4916 (1996).
- <sup>16</sup>K. Imai, *Solid-State Electron.* **24**, 159 (1981).
- <sup>17</sup>M. B. H. Breese, F. J. T. Champeaux, E. J. Teo, A. A. Bettoli, and D. J. Blackwood, *Phys. Rev. B* **73**, 035428 (2006).
- <sup>18</sup>S. Azimi, J. Song, Z. Y. Dang, H. D. Liang, and M. B. H. Breese, *J. Micromech. Microeng.* **22**, 113001 (2012).
- <sup>19</sup>P. Yang, G. Mashanovic, I. Gomez-Morilla, W. H. G. Reed, E. J. Teo, D. Blackwood, M. B. H. Breese, and A. A. Bettoli, *Appl. Phys. Lett.* **90**, 241109 (2007).
- <sup>20</sup>Z. Y. Dang, M. B. H. Breese, G. Recio-Sánchez, S. Azimi, J. Song, H. Liang, A. Banas, V. Torres-Costa, and R. J. Martín-Palma, *Nanoscale Res. Lett.* **7**, 416 (2012).
- <sup>21</sup>T. R. Oldham, *IEEE Trans. Nucl. Sci.* **31**, 1236 (1984).
- <sup>22</sup>T. R. Oldham and F. B. McLean, *IEEE Trans. Nucl. Sci.* **50**, 483 (2003).
- <sup>23</sup>A. G. Foyt, W. T. Lindley, C. M. Wolfe, and J. P. Donnelly, *Solid-State Electron.* **12**, 209 (1969).
- <sup>24</sup>L. S. Lee, C. Liao, T.-H. Lee, D. D.-L. Tang, T. S. Duh, and T.-T. Yang, *IEEE Trans. Electron Devices* **48**, 928 (2001).
- <sup>25</sup>S. M. Myers, G. A. Petersen, and C. H. Seager, *J. Appl. Phys.* **80**, 3717 (1996).
- <sup>26</sup>A. Peeva, R. Kögl, W. Skorupa, J. S. Christensen, and A. Yu. Kuznetsov, *J. Appl. Phys.* **95**, 4738 (2004).
- <sup>27</sup>R. Kögl, A. Peeva, A. Mücklich, F. Eichhorn, and W. Skorupa, *Appl. Phys. Lett.* **88**, 101918 (2006).
- <sup>28</sup>E. Colombo, A. Bosio, S. Calusi, L. Giuntini, A. Lo Giudice, C. Manfredotti, M. Massi, P. Olivero, A. Romeo, N. Romeo, and E. Vittone, *Nucl. Instrum. Methods Phys. Res. B* **267**, 2181 (2009).
- <sup>29</sup>N. P. Economou, J. A. Notte, and W. B. Thompson, *Scanning* **34**, 83 (2012).
- <sup>30</sup>A. J. Steck, J. Xu, H. C. Mogul, and S. Mogren, *Appl. Phys. Lett.* **62**, 1982 (1993).
- <sup>31</sup>I. S. Chun, E. K. Chow, and X. L. Li, *Appl. Phys. Lett.* **92**, 191113 (2008).
- <sup>32</sup>J. F. Ziegler, M. D. Ziegler, and J. P. Biersack, *Nucl. Instrum. Methods Phys. Res. B* **268**, 1818 (2010).
- <sup>33</sup>J. F. Ziegler, J. P. Biersack, and U. Littmark, *The Stopping and Range of Ions in Solids* (Pergamon, New York, 2003).
- <sup>34</sup>M. B. H. Breese, D. N. Jamieson, and P. J. C. King, *Materials, Analysis Using a Nuclear Microprobe* (Wiley, New York, 1996).
- <sup>35</sup>K. Irmscher, H. Klose, and K. Maass, *J. Phys. C* **17**, 6317 (1984).
- <sup>36</sup>H. Matsuura, T. Ishida, T. Kirihata, O. Anzawa, and S. Matsuda, *Jpn. J. Appl. Phys., Part 1* **42**, 5187 (2003).
- <sup>37</sup>M. Petris, *1999 International Semiconductor Conference, CAS'99 Proceedings* (IEEE, 1999), Vol. 1, p. 393.
- <sup>38</sup>B. G. Svensson, B. Mohadjeri, A. Hallen, J. H. Svensson, and J. W. Corbett, *Phys. Rev. B* **43**, 2292 (1991).
- <sup>39</sup>B. G. Svensson, C. Jagadish, A. Hallen, and J. Lalita, *Nucl. Instrum. Methods Phys. Res. B* **106**, 183 (1995).
- <sup>40</sup>A. Hallen, N. Keskitalo, F. Masszi, and V. Nagi, *J. Appl. Phys.* **79**, 3906 (1996).